hydrogen

MDPI

Article

Comparison of the Temperature, Radiation, and Heat Flux Distribution of a Hydrogen and a Methane Flame in a Crucible Furnace Using Numerical Simulation

Alexander Mages [1,2,*] and Alexander Sauer [1,2]

[1] Fraunhofer Institute for Manufacturing Engineering and Automation IPA, 70569 Stuttgart, Germany
[2] Institute for Energy Efficiency in Production (EEP), University of Stuttgart, 70569 Stuttgart, Germany
* Correspondence: Alexander.Mages@eep.uni-stuttgart.de; Tel.: +49-711-970-3679

Abstract: Sustainable technologies to replace current fossil solutions are essential to meet future CO_2 emission reduction targets. Therefore, this paper compares key performance indicators of a hydrogen- and a methane-flame-fired crucible furnace with computational fluid dynamics simulations at identical firing powers, aiming to fully decarbonize the process. Validated numerical models from the literature were used to compare temperatures, radiation fields, radiation parameters and heat transfer characteristics. As a result, we observed higher combustion temperatures and a 19.0% higher fuel utilization rate in the hydrogen case, indicating more efficient operating modes, which could be related to the increased radiant heat flux and temperature ranges above 1750 K. Furthermore, higher scattering of the heat flux distribution on the crucible surface could be determined indicating more uneven melt bath temperatures. Further research could focus on quantifying the total fuel consumption required for the heating up of the furnace, for which a transient numerical model could be developed.

Keywords: combustion; hydrogen; industrial furnace; energy efficiency

Citation: Mages, A.; Sauer, A. Comparison of the Temperature, Radiation, and Heat Flux Distribution of a Hydrogen and a Methane Flame in a Crucible Furnace Using Numerical Simulation. *Hydrogen* **2024**, *5*, 459–473. https://doi.org/10.3390/hydrogen5030026

Academic Editors: Bahman Shabani and Mahesh Suryawanshi

Received: 19 June 2024
Revised: 13 July 2024
Accepted: 18 July 2024
Published: 21 July 2024

1. Introduction

To meet the CO_2 reduction targets of the Paris Agreement on climate change, countries around the world are developing strategies to produce hydrogen and apply it in the industrial, mobility, and energy sectors [1,2]. Therefore, the USA is aiming to halve its green house as emissions by 2030 compared to 2005 levels and achieve complete climate neutrality by 2050 [3]. Furthermore, all countries within the EU are legally obligated to reduce their carbon emissions to 55% of 1990 levels by 2030 and to achieve climate neutrality by 2050 [4]. In 2021, the German government set even more ambitious targets to reduce greenhouse gas emissions by 65% by 2030 and 88% by 2040 compared to 1990 levels and to achieve climate neutrality by 2045 [5]. Increasing energy efficiency is seen as a fundamental pillar of the energy transition along with the expansion of renewable energies, as it requires less energy infrastructure to operate production processes [6] (p. 7) [7].

With an annual energy consumption of 4.2 TWh and estimated total emissions of 1.8 million tons of CO_2-equivalent, non-ferrous metal foundries (abbreviated as NF-metal foundries) are among the particularly energy- and emission-intensive industries, with the larger share of 2.4 TWh being provided by fossil fuels. Additionally, 50% of the total energy consumption is attributed to the melting process [8] (p. 1) [9]. Green hydrogen enables the partial or complete reduction of greenhouse gas emissions through the blending or complete substitution of fossil fuels.

However, integrating hydrogen into energy systems presents several challenges. In Ref. [10], the authors evaluated over 59 field projects and 33 stakeholder dialogues, identifying five barrier domains (technical, infrastructural, socioeconomic, environmental, and institutional) which need to be overcome for the Netherlands. Focusing on the technical

domain, challenges in efficiency and durability on the component level are mentioned. In the case of fuel-fired thermal processing plants, this may require adjustments on the burner unit or combustion chamber, as hydrogen combustion is associated with higher fuel volume flows at identical firing rates, higher reactivity, and higher adiabatic flame temperatures [11]. Therefore, challenges such as significantly increased NOx emissions and material resistance at high temperatures may occur [12] [13] (pp. 8–28) [14].

Crucible furnaces are mainly used in NF-metal foundries and currently operate electrically or with fossil fuels. Switching to hydrogen thus presents significant potential for reducing CO_2 emissions in NF-metal foundries [15]. Computational fluid dynamics (CFD) simulations can help to identify energy-saving potentials and to make design decisions, such as adapting the geometry to the changed requirements of a hydrogen flame [16] (pp. 8–10) [17] (p. 117) [18] (p. 21). In Ref. [19], a literature review on CFD simulations of fuel-fired crucible furnaces was conducted, resulting in the identification and assessment of models for fossil-fired crucible furnaces with varying modelling quality.

A comparison of key performance indicators by changing the fuel composition to hydrogen, however, has not yet been carried out, but due to substantially different combustion characteristics, significant changes on these can be expected [13]. High energy utilization rates and even heat distributions on the crucible surface are desired to achieve uniform melt bath temperatures and minimal thermal stresses within the materials [20]. Therefore, in this paper, two CFD models—one for a hydrogen and a second for a methane flame in a crucible furnace designed for fossil fuels—are set up, and key performance indicators at identical firing powers are compared.

To do so, at first, typical crucible furnace operating conditions are described, from which the case study is derived. Then, based on literature research for jet and swirl burners for methane and hydrogen flames, applicable numerical models are selected, and the simulation setup is placed in the context of real operating modes. Subsequently, temperature and radiation fields, radiation parameters, and heat transfer characteristics are evaluated to support hydrogen-related design decisions within the crucible furnace and burner unit.

2. Furnace Case Study and Numerical Modelling

In this section, combustion models representing methane and hydrogen flames in jet and swirl burners are researched and evaluated. Then, the case study is described, and the numerical simulation model of the crucible furnace, considering its operational characteristics, is described.

2.1. State of the Art in Modelling Natural Gas, Methane, Hydrogen, and Hydrogen-Blended Flames in Jet and Swirl Burners

A literature review was conducted on the numerical simulation of jet and swirl burners to select numerical models, capable of describing methane and hydrogen flames for the case study. Numerous publications successfully use numerical methods to describe temperature, flow, and species fields for a wide range on burners for natural gas (NG), methane, hydrogen, and hydrogen-blended flames. The Reynolds-averaged Navier–Stokes equations (RANS equations) are commonly employed using turbulence and combustion models for solving these simulations.

In Refs. [21,22], the authors simulate jet burners with varying hydrogen–natural gas compositions using the RANS approach and validate the results against experimental data.

In Ref. [21], combustion is modelled using a combined finite-rate and eddy break-up model, the second one uses a flamelet approach with assumed probability density functions. The first publication employs the standard k-ε, the renormalization group k-ε (RNG), and the Reynolds stress model, finding that all turbulence models have similar axial profiles and are therefore suitable for describing the flame. Radiation is modeled using the P1 radiation model. Validation was performed on measurement data evaluating the maximum temperature of the hydrogen flame, exhaust gas temperatures for H_2 and CH_4

as well as the exhaust gas composition showing overall adequate results except for the CH_4 exhaust gas temperature which was predicted to low. The authors attribute the deviation to a slightly different location of the measurement point compared to the simulation and model inaccuracies.

The latter publication applies the standard k-ε-, the Reynolds stress, as well as a modified k-ε turbulence model. Validation was performed for the CH_4 flame with three radial temperature profiles at different combustion chamber depths. The results show that all models describe the temperature profiles as qualitatively adequate, with the modified k-ε turbulence model providing the most accurate results. If and which radiation model was used is not described.

In Refs. [23–26], the combustion of variable hydrogen fractions in different swirl burners is simulated, validated, and evaluated. To describe the turbulence, the first publication applies the Realizable k-ε and the RNG models, yielding better results for the former. Furthermore, the authors state that in principle, both models are applicable to the slow-swirling flow in their case. The discrete ordinate method has been used for the radiation modelling and the eddy dissipation combustion model, with adjusted reaction mechanisms for the different fuel compositions used. The simulation data were compared with temperature and exhaust gas composition measurements at the outlet for the natural gas case yielding a temperature deviation of about 14%.

In Ref. [24] the authors use the coupled finite-rate and eddy break-up model to describe the combustion, the standard k-ε as well as the RNG model for the turbulence, and the discrete ordinate method for radiation. In their validation, they compare the temperature fields of different hydrogen contents in a cross section, with measurement data showing that both models can describe the flame structure with more accurate results for the RNG model.

To describe the turbulence, the authors in Ref. [25] use the RNG model, the combustion is modeled with a finite rate approach, and the radiation is represented with the P1 model. They successfully validate their results with temperature measurements at the flame center.

In Ref. [26], a 100% natural gas flame and a mixture containing 30% hydrogen are simulated, applying different flamelet approaches as well as the realizable k-ε and the Reynolds stress turbulence models. If and which radiation model was used is not described. The simulation results were validated against flow patterns, radial temperature profiles, and exhaust gas concentrations, yielding the most accurate results with the partially premixed combustion and the Reynolds stress turbulence model.

In Table 1, the numerical methods used for describing the flames and the maximum temperatures are summarized. In summary, the temperature and flow fields of the mentioned fuel mixtures in jet and swirl burners can be simulated using the RANS equations in combination with the coupled finite-rate eddy dissipation or flamelet approach as well as the P1 or discrete ordinates radiation model. For swirl burners, models such as the Realizable k-ε or Reynolds stress model, which deviate from the standard k-ε Model, provide more accurate results in swirling flows. In all publications, an increase in hydrogen fraction is observed to result in higher combustion chamber temperatures and NOx emissions, while CO_2 emissions decrease.

Table 1. Numerical models used to describe temperature, flow, and species fields of various jet and swirl burners.

Literature	Burner Type	Fuel Composition	Turbulence Model	Radiation Model	Combustion Model	Max. Temperatures in K	Validation
[21]	Jet	H_2-NG compositions (0–100%)	Standard k-ε Renormalization Group k-ε Reynolds stress	P-1 radiation	Coupled Finite-Rate and eddy break-up	100% H_2: 2325 100% CH_4: 2012	Experimental data

Table 1. *Cont.*

Literature	Burner Type	Fuel Composition	Turbulence Model	Radiation Model	Combustion Model	Max. Temperatures in K	Validation
[22]	Jet	H_2-NG compositions (0–50%)	Modified k-ε	Not mentioned	Flamelet	Not evaluated	Exp. data and num. results in literature
[23]	Swirl	H_2-NG compositions (0–100%)	Realizable k-ε	Discrete Ordinates	Eddy dissipation	100% H_2: ~2345 100% NG: 2174	Experimental data
[24]	Swirl	H_2-CH_4 compositions (0–100%)	Standard k-ε Renormalization Group k-ε	Discrete Ordinates	Coupled Finite-Rate and eddy break-up	Not evaluated	Experimental data
[25]	Swirl	NG-Synfuel and variable H_2 contents	Renormalization Group k-ε	P-1 radiation	Finite-Rate	80% H_2: ~2380 40% H_2: ~2110	Experimental data
[26]	Swirl	100% NG and 30% H_2 in NG	Realizable k-ε Reynolds stress	Not mentioned	Flamelet	Not evaluated	Experimental data

2.2. Case Study of the Fuel Fired Crucible Furnace

Figure 1 illustrates the internal contours of the considered crucible furnace in the front and side views, including inlets, outlets, burner positioning, and used burner heads to generate the computational domain for both simulations. The geometry was obtained by simplifying the CAD of a conventional fossil fired crucible. Additionally, the inlet and outlet surfaces on which the boundary conditions were applied are marked. As can be seen in both cases, the same inlet areas are used for air and gas. On the remaining surface, wall boundaries were applied. Such a furnace can be used for melting or holding metals warm and is operated in batch mode for aluminum. During the melting process, the furnace melts the metal at high power and overheats it to 680 °C before keeping it warm at a lower power or removing it for further processing by tilting or ladling. Due to the many time-varying parameters, the furnace operation is considered transient. The burner unit can regulate the target temperature through pulsation or power modulation [15] [27] (p. 321) [28]. As shown in Figure 1, the fuel gas flows separately from the air through the burner tube and is distributed into the combustion chamber through the nozzle head. The air is injected around the burner head and through corresponding holes. Therefore, fuel and oxidizer are mixed near the nozzle head and downstream until the ignition limit is reached, triggering the combustion reaction and flame formation. To avoid excessive temperatures in the vicinity of the nozzle head, the air holes for mixing were removed in the hydrogen case.

To compare both flames, identical steady-state operating points with the same heating power were selected at a melt bath temperature of 680 °C. This approach neglects time-dependent factors such as thermal masses in the furnace, including walls, burners, and other components. Thus, the simulation represents approximately a snapshot at the end of the melting process when the temperature in the melt bath reaches 680 °C. At this point, the burner operates at its maximum heating power of 150 kW at $\lambda = 1.1$ using either methane or hydrogen before transitioning to the holding operation mode or removing the molten material.

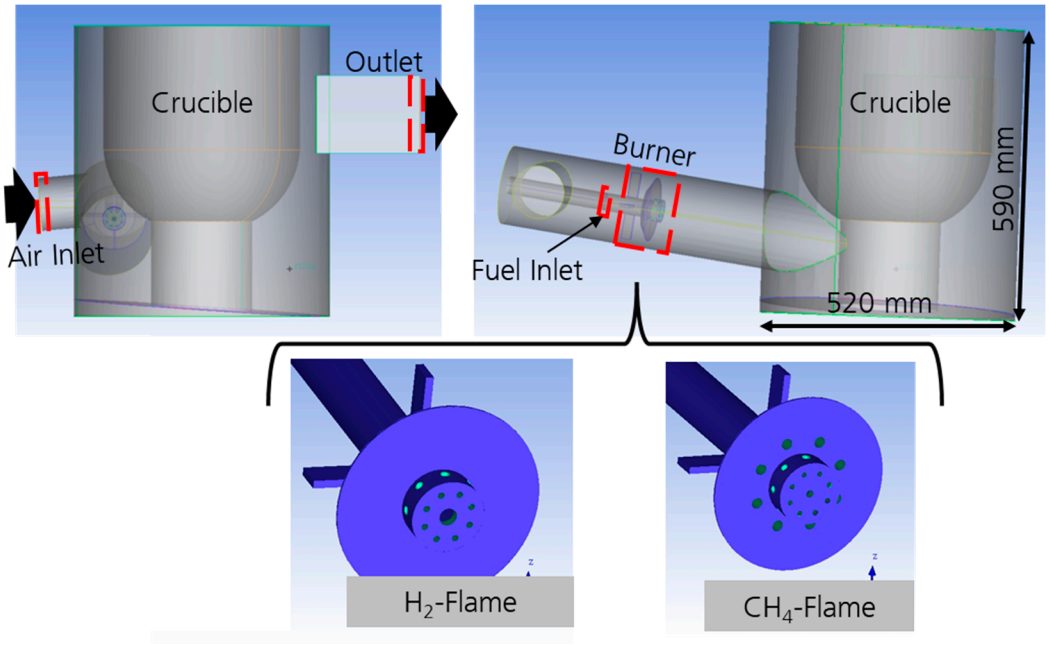

Figure 1. Computational domain with dimensions, inlet and outlet boundaries, burner positioning, and burner heads (**left**: hydrogen, **right**: methane) used in the simulation which was obtained by simplifying the CAD of a conventional fossil fired crucible.

2.3. Numerical Setup

Two CFD models were developed and simulated to compare both combustion cases; the corresponding computational domains are shown in Figure 1. The RANS equations were discretized using the finite volume method and solved using the commercial flow solver ANSYS Fluent®. As shown in Section 2.2, this simulation methodology is widely used in combustion simulations, including for melting furnaces [21,23,26,29–31].

It is necessary to consider not only the turbulent flow field but also the chemical processes to predict turbulent non-premixed flames formed by the mixing of a fuel and air stream through flow and turbulence. The large number of involved species and interactions between turbulent fluctuations in the flow field and chemical kinetics significantly increase the computational effort, which is why generally simplified models with limited validity are used for calculations [32] (pp. 343–416) [33] (p. 38). As described in Section 2.2, the flamelet model, among others, has been successfully used in the literature to describe hydrogen and methane flames. This approach assumes that the turbulent non-premixed flame can be represented as an ensemble of local laminar flames called flamelets. These, in turn, can be efficiently calculated from the conservation equations of a one-dimensional counterflow flame in a pre-processing step and tabulated, taking extensive reaction mechanisms into account. The chemistry–turbulence interaction in the reaction rate is modelled with assumed probability density functions. Due to its computational efficiency and the ability to consider chemistry–turbulence interaction via reaction mechanisms, this model was selected [22,26,34]. In ANSYS Fluent, the non-premixed combustion model with a diabatic steady-state diffusion flame was accordingly chosen. For the methane flame, the internal GRI 3.0 mechanism was used, and for the hydrogen flame, the hydrogen reaction mechanism was used.

To close the Reynolds stress tensor, the standard k-ε turbulence model was chosen, and the enhanced wall treatment was selected to describe the flow near walls. This is a two-layer model that maps the boundary layer using empirical wall functions depending on the dimensionless wall distance y+ or resolves it explicitly. This allows the (turbulent) viscosity, the (turbulent) dissipation rate ε, and the velocity gradients to be explicitly calculated near the wall, which, for example, allows for a more accurate prediction of heat transfer [35] (pp. 369–389).

Radiation is modelled using the discrete ordinates model, which transforms the radiative transfer equation into a transport equation for radiation intensity and solves it for a finite number of radiation directions. Additionally, the combustion products H_2O and CO_2 participate in the radiation exchange through absorption and emission and must be considered in the calculations. For this purpose, the weighted sum of gray gases model (Abr. WSGGM) is used, which has established itself in combustion simulations as a compromise between computational time and accuracy [32] (p. 442).

Spatially, the gradients were discretized using the Green–Gauss cell-based method, pressure with the PRESTO! scheme, and all other variables with the second-order upwind scheme. The pressure-based solver was used for solving, and the SIMPLE scheme was employed for the pressure-velocity coupling. The convergence criterion was set to 10^{-3} for the mass, momentum, turbulence, and mixture fraction equations and to 10^{-6} for the energy and radiation equations [36] (pp. 952+954).

Below the equations for species, momentum, energy and radiation are depicted, which are solved with above described modelling:

$$\frac{\partial \varrho}{\partial t}(\rho Y_i) + \nabla \left(\varrho \vec{v} Y_i \right) = -\nabla \vec{J}_i + R_i \tag{1}$$

$$\frac{\partial}{\partial t}\left(\rho \vec{v}\right) + \nabla \left(\varrho \vec{v}\vec{v} \right) = -\nabla p + \nabla \left(\bar{\bar{\tau}}\right) + \rho \vec{g} + \vec{F} \tag{2}$$

$$\frac{\partial}{\partial t}\left(\rho(e + \frac{v^2}{2})\right) + \nabla\left(\varrho \vec{v}(h + \frac{v^2}{2})\right) = \nabla(k_{eff}\nabla T - \sum_j h_j \vec{J}_i + (\bar{\bar{\tau}}_{eff}\ \vec{v})) + S_h \tag{3}$$

$$\frac{dI\left(\vec{r}, \vec{s}\right)}{ds} + (a + \sigma_s) I\left(\vec{r}, \vec{s}\right) = a \cdot n^2 \frac{\sigma\, T^4}{\pi} + \frac{\sigma_s}{4\,\pi} \int_0^{4\,\pi} I\left(\vec{r}, \vec{s}'\right) \Phi\left(\vec{s}, \vec{s}'\right) d\Omega' \tag{4}$$

where ϱ is the density, Y_i the species fraction, $\vec{v}$ the velocity vector, $\vec{J}_i$ the diffusion flux, R_i the net chemical rate of production of species i, p the pressure, $\bar{\bar{\tau}}$ the stress tensor, $\vec{g}$ the gravitation, $\vec{F}$ external body forces, e the internal energy, h the enthalpy k_{eff} the effective conductivity, T the temperature, and S_h the volumetric source term. Furthermore, I represents radiation intensity, $\vec{r}$ position, $\vec{s}$ direction, $\vec{s}'$ scattering direction vector, s as path length, a as absorption, σ_s as scattering coefficient, n as refractive index, σ as Stefan–Boltzmann constant, Φ as phase function, and Ω' as solid angle [36] (pp. 3+160+174+224).

2.4. Boundary Conditions

To solve the posed boundary value problem, all boundary conditions must be defined. Therefore, the exterior walls and the crucible inner walls in contact with the melt were chosen. The explicitly modelled domain describes the inner volume of the furnace, while the external walls or the wall thickness of the crucible up to the melt are taken into account through internal shell elements of the program. Material properties and wall thicknesses can be assigned to these, with which the steady-state heat flows through the walls are described. The corresponding boundary conditions, wall thicknesses, and materials are given in Tables 2 and 3, which describe the 150 kW heating cases at 680 °C melt temperature. In addition, the melt bath is not modelled explicitly but is represented by a constant inner wall temperature. This neglects temperature fluctuations and free convection effects in the melt, which is assumed to have a minor impact compared to the comparison of hydrogen and methane flames.

Table 2. Boundary conditions for the simulation cases.

	Inlet Air	Inlet Gas	Wall Crucible	Wall (Bottom)	Wall (Sides)	Wall (Top)	Wall (Outlet)	Wall (Burner Inlet)
Velocity (m/s) *	5.8/4.9	4.9/16.2	x	x	x	x	x	x
Temperature (K)	303	323	953	353	x	x	x	x
Temp. of the free flow (K)	x	x	x	x	303	303	303	303
Heat transfer coefficient ** ($W/(m^2K)$)	x	x	x	x	4	5.2	5,2	2,9

* Methane/Hydrogen; ** Calculated with free convection Nusselt correlations for cylinders and plate geometries according to [37].

Table 3. Applied wall material properties and thicknesses in the shell elements.

		Wall Crucible		Wall (Bottom)		Wall (Sides)		Wall (Top)		Wall (Outlet)		Wall (Burner Inlet)	
Shell 1	SynCarb	ρ	2200	Chamotte	ρ 2030	Chamotte	ρ 2030	Chamotte	ρ 2030	Stone	ρ 2450	Chamotte	ρ 2030
		λ	28		λ 0.97		λ 0.97		λ 0.97		λ 1.74		λ 0.97
		ε	0.6		ε 0.7		ε 0.7		ε 0.7		ε 0.7		ε 0.7
		s	0.035		s 0.093		s 0.101		s 0.065		s 0.067		s 0.101
Shell 2		x		Vermiculit	ρ 600	Vermiculit	ρ 600	Steel S235	ρ 7850	Vermiculit	ρ 600	Vermiculit	ρ 600
					λ 0.2		λ 0.2		λ 58		λ 0.2		λ 0.2
					ε -		ε -		ε -		ε -		ε -
					s 0.05		s 0.05		s 0.005		s 0.04		s 0.05
Shell 3		x		Steel S235	ρ 7850	Promalight	ρ 350	x		Steel S235	ρ 7850	Promalight	ρ 350
					λ 58		λ 0.036				λ 58		λ 0.036
					ε -		ε 0-				ε -		ε 0-
					s 0.005		s 0.02				s 0.005		s 0.02
Shell 4		x		x		Steel S235	ρ 7850	x		x		Steel S235	ρ 7850
							λ 58						λ 58
							ε -						ε -
							s 0.005						s 0.005

ρ: Density in kg/m^3; λ: thermal conductivity in $W/m\,K$; emissivity: ε in -; wall thickness: s in m; based on specific manufacturing data sheets.

2.5. Mesh Independence Study

Applying a mesh independence study for the hydrogen case with three uniformly refined meshes, the dependency of the solution to the mesh was evaluated. Calculations were performed on the high-performance computer system of Baden-Württemberg's Universities and Universities of Applied Sciences bwUniCluster 2.0. In Figure 2, the volume and surface mesh of the outlet plane of the second refinement level are depicted, and they consist of about 2.6×10^7 nodes and 7.5×10^6 cells, respectively. In addition, on the lower right side, the contours of the burner with the air and gas inlets are shown. For uniformly coarser meshes below $1*10^7$, the convergence limits could not be reached. The mesh resolution is considered sufficiently accurate if no change can be seen in the solution upon further refinement. The total heat transfer into the crucible and the average temperature of the outlet plane were chosen as control quantities and are depicted in Figure 3. As can be observed, only minor changes for both maximum quantities—1% and below to the finest mesh—can be stated, and therefore, all meshes identify as sufficiently accurate to describe the control quantities. As a compromise between solution accuracy and stability, as well as computational resources, the second mesh is used in the subsequent investigation.

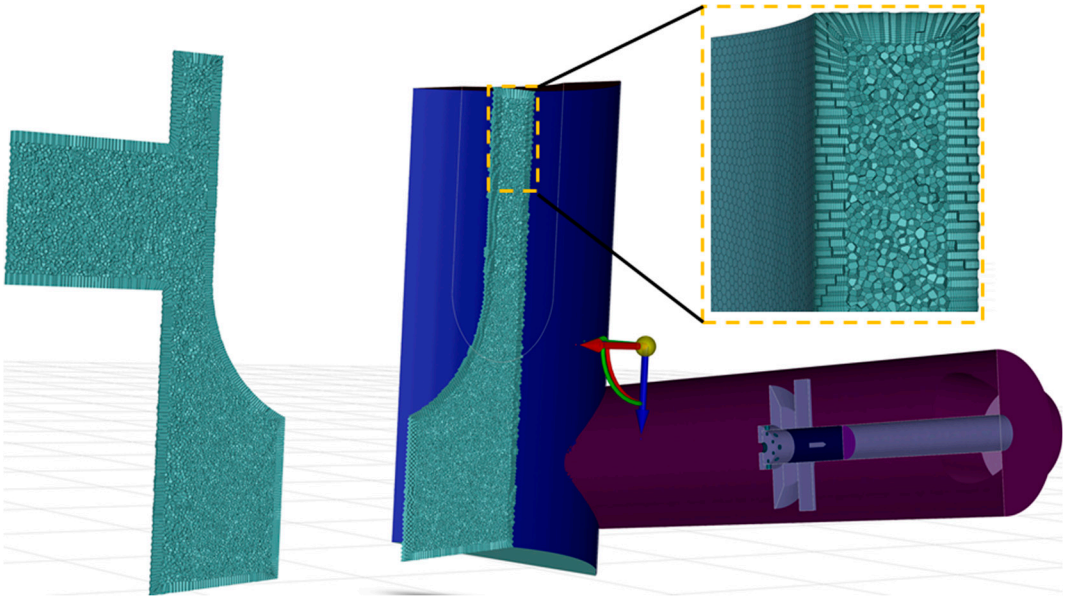

Figure 2. Cut plane of the volume and surface mesh of the second refinement level at the outlet plane and inlet area, respectively.

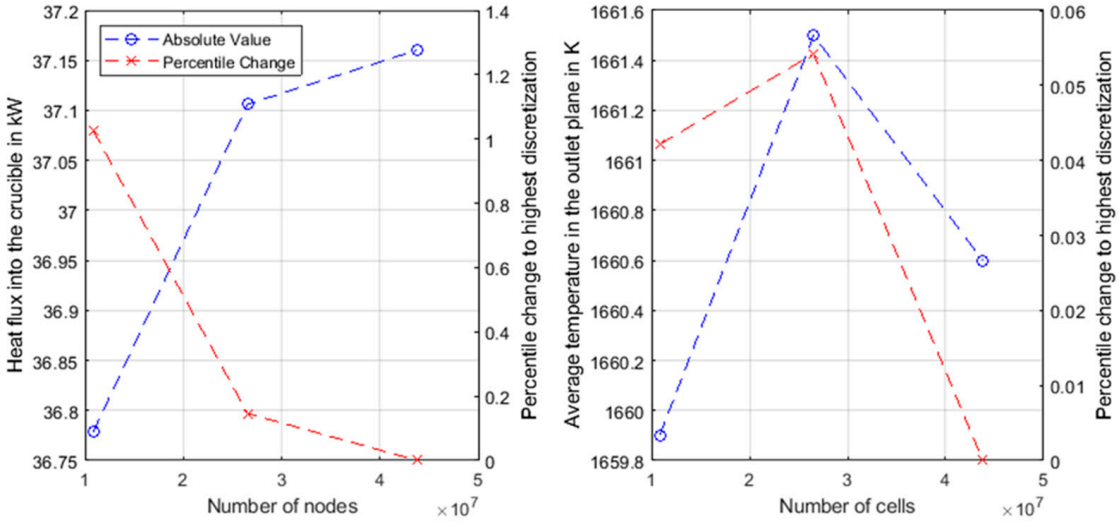

Figure 3. Change in total heat flux into the crucible (**left**) and the average temperature of the outlet plan (**right**) of the mesh independence analysis for two target quantities heat flux into the crucible and the average temperature of the outlet plane for three.

3. Evaluation

In the following, the combustion characteristics of the methane and hydrogen flame with previously described numerical setup, and operating conditions are compared by evaluating temperature and radiation fields as well as radiation parameters. Furthermore, the results are plausibilized with the literature in Section 2.1. Then, the energy utilization rates and heat distributions are analyzed, identifying as one of the key performance indicators for the furnace operation. Therefore, the total convective and radiative heat fluxes, as well as the heat distribution into the crucible, were compared and related to the changed combustion characteristics. Finally, the results are discussed in the context of furnace design and burner adjustments.

3.1. Characterization and Comparison of the Temperature Fields the Methane and Hydrogen Flames

Figure 4 depicts the temperature fields of the inlet and outlet cross sections for the hydrogen and methane flames as well as the volume-averaged temperatures. Additionally, regions of the crucible furnace are divided into the areas inlet, outlet, front side, and back side. To evaluate both simulations, in Table 4, the temperatures were initially classified as either medium or high and then compared qualitatively.

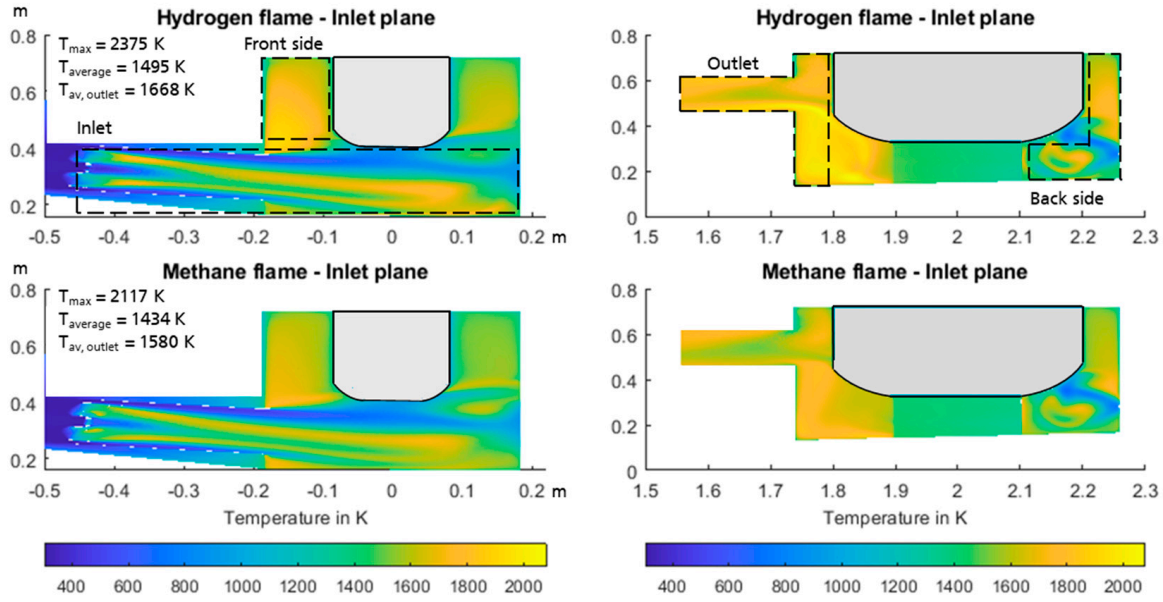

Figure 4. Temperature fields of the inlet and outlet sides of the hydrogen flame (**top**) and the methane flame (**bottom**).

Table 4. Qualitative classification and comparison of the temperature fields of both flames.

Area	Inlet	Outlet	Front	Back
Qualitative	Medium	High	High	Medium
Hydrogen	Equal	Higher	Higher	Equal
Methane	Equal	Lower	Lower	Equal

Overall, a similar combustion characteristic of both flames can be observed. The reactants begin to mix in the inlet area, forming a reaction zone with strong temperature gradients that continues around the back side of the crucible. Further downstream on the outlet side, the highest temperatures and homogenization of the temperature profile across the cross-section can be observed. At this point, a small part of the flow directly exits the furnace space, leading to very high temperatures in the outlet area and indicating possible approaches for optimizing the furnace geometry. The larger flow portion continues around the crucible, where further homogenization and a slight decrease in temperatures can be seen. Subsequently, the flow leaves the combustion chamber via the outlet.

Comparing both flames, similar temperature fields with slightly higher temperatures and broader reaction zone of the hydrogen flame can be observed in the inlet area and on the back side. Further downstream around the crucible on the outlet side, the temperature rises by about 200 K above that of the methane flame due to the higher flame temperatures of hydrogen. Overall, an increase in the average combustion chamber temperature of 61 K from 1434 K in the case of methane to 1495 K for the hydrogen flame can be observed, which is largely attributable to the outlet and front side downstream.

To verify the simulation setup, the maximum flame temperatures and the combustion characteristics are compared with the literature in Table 1. As a result, similar maximum

temperatures for the hydrogen and methane flames were observed, ranging between the lowest and highest maximum flame temperatures. In addition, the maximum temperature increases by about 258 K when switching to hydrogen, which is also within the range attested in the literature.

Comparing the flame characteristic by switching to hydrogen, all authors claim an increase in temperature due to the higher adiabatic flame temperature, which is also observed in Figure 4. Ref. [23] describes a longer, broader flame in more detail as well as increased radial temperatures with increasing hydrogen content, which we also observe (Figure 4).

As a result, comparing the maximum temperatures and the changed combustion characteristics, both flames presented are within a plausible range. Deviations within that range seem plausible and may occur due to different numerical setups, boundary conditions, burner or combustion chamber geometry.

3.2. Characterization and Comparison of the Radiation Characteristics the Methane and Hydrogen Flame

Looking at the net radiation power of the gases in Figure 5, patterns similar to the temperatures can be seen. In areas of low temperatures, low or negative net radiation powers can be observed, indicating a decrease in radiation intensity, whereas in areas of high temperatures, high net radiation powers of the gases can be observed, which is reflecting the strong temperature dependence of radiative heat exchange.

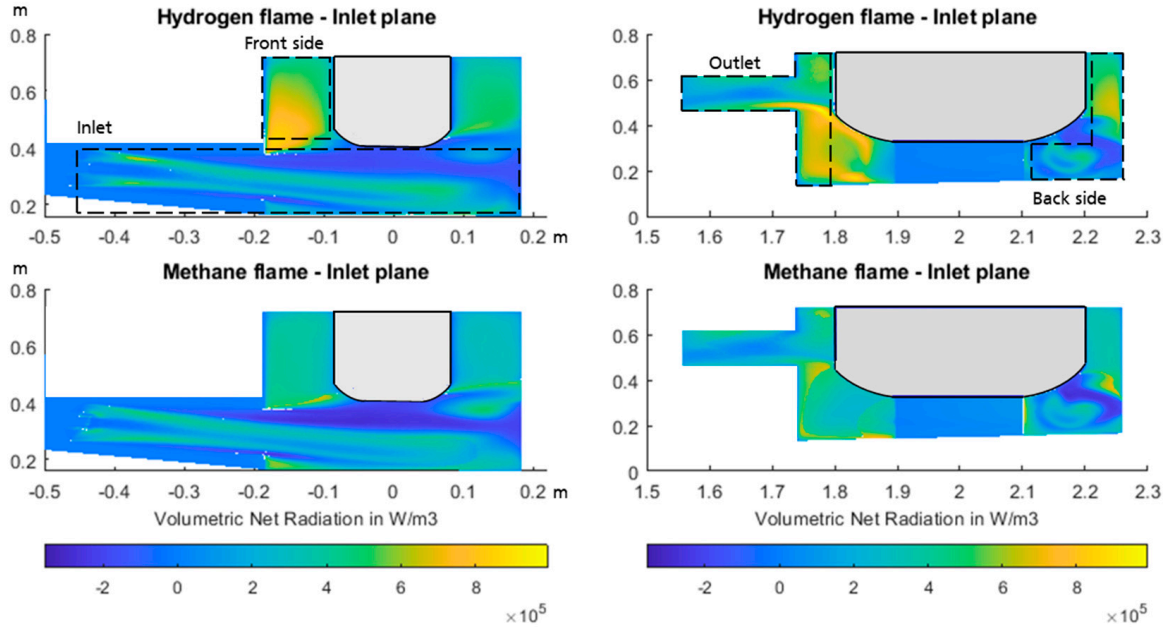

Figure 5. Net radiation power of the inlet and outlet sides of the hydrogen flame (**top**) and the methane flame (**bottom**).

Figure 5 shows the corresponding absolute absorption, emission, and net radiation powers across the temperature quantiles. For both flames, up to about the 50% temperature quantile, the absorption rates exceed the emission rates, indicating a decrease in radiation intensity. Consequently, in these cells, net radiation heat is absorbed by the gas. Beyond that, the emission rates dominate due to the significantly stronger temperature than absorption dependency, resulting in a sharply increased radiation power with rising temperature. Thus, the regions of the inlet area and the back side can be associated with comparatively low net heat radiation, with the highest found in the outlet and front side area.

Comparing the emission and absorption behavior of both flames in Figure 6 (top), higher emission and absorption rates can be observed for the methane flame at the respective temperature quantiles. With increasing temperature quantiles, both ratios decrease

continuously, and at the 85% quantile, the emission rates of the hydrogen flame exceed those of the methane flame. Overall, up to the 0.8% temperature quantile, the different radiation characteristics do not lead to any change in the net radiation behavior. From there, the hydrogen flame tends to emit more net power at each quantile.

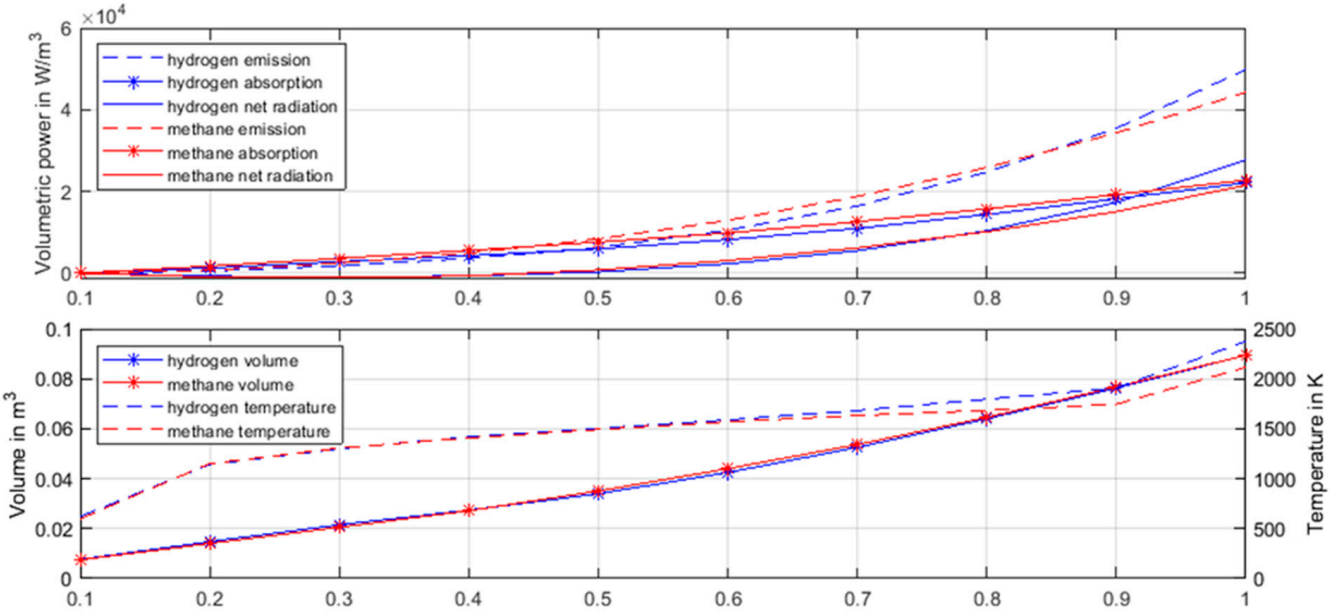

Figure 6. Temperature quantiles (**bottom**) and corresponding absolute absorption and emission rates (**top**), net radiation powers (**top**), and volume (**bottom**) of both flames.

According to the radiative transfer equation and by neglecting scattering effects, the change in radiation intensity depends on temperature as well as emission and absorption coefficients. Therefore, temperature quantiles and the associated volume are shown in Figure 6 (bottom). As seen, the respective temperature quantiles of both flames occupy the same volumes, with an over-proportional rise in temperatures for the hydrogen flame from approximately the 60% temperature quantile, indicating smaller emission and absorption coefficients for the hydrogen case at the same temperature. Due to the similar temperature fields of both flames, the temperature ranges occupy approximately the same regions. Between the 0.6–0.8 quantiles, higher temperatures are needed for the same net emission, which then turns into higher net emission rates for further rising temperatures. Therefore, higher net radiation powers occur mainly in areas of high temperatures above ~1750 K in the hydrogen case. The difference in net radiation powers of both flames correlates with the temperatures, suggesting a linear relationship. Consequently, the increased net radiation can be almost exclusively related to higher temperatures than the methane flame.

3.3. Characterization and Comparison of the Crucible Heat Input of the Methane and Hydrogen Flames

Apart from a high total heat transfer rate into the crucible, which describes the energy utilization at the simulated operating point, an even heat distribution on the crucible surface is desired since a uniform melt bath temperature and minimal thermal stresses are promoted. Therefore, the following evaluation of energy utilization is based on the transferred absolute radiation and convective heat flux (Figure 7, bottom7). For the even heat distribution, the spatial distribution of the heat flux density, its statistical moments, and the associated histogram are analyzed (Figure 7, top).

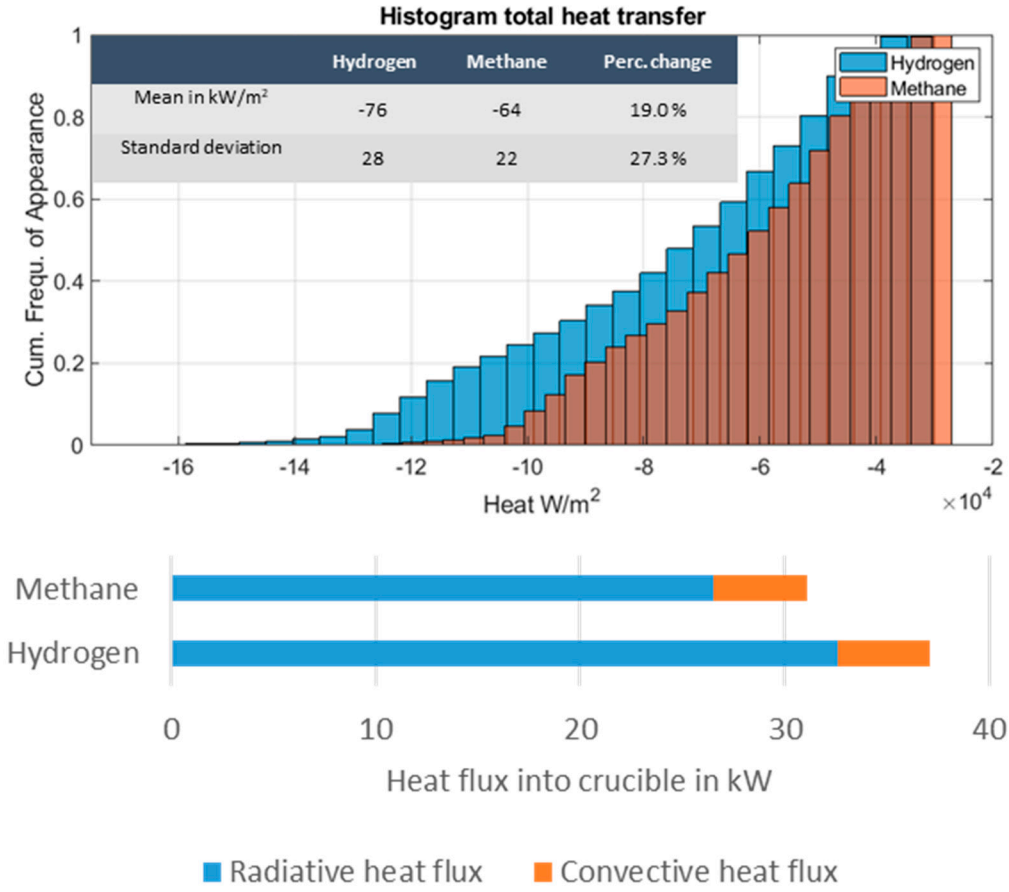

Figure 7. Heat flux distribution function with mean value and standard deviation (**top**) as well as transferred convective and radiative heat fluxes.

At the bottom of Figure 7, an overall increase of the total heat transfer by 19.0% for the hydrogen flame can be observed, indicating a significantly enhanced energy utilization of the fuel, which is almost exclusively due to an increased radiant heat share. The convective portion remains nearly constant (hydrogen: 4.5 kW, methane: 4.6 kW) and plays a minor role in heat transfer for both flames (hydrogen: 12.1%, methane: 14.8%).

The heat transfer on the crucible surface is similar for both flames (cf. Figure 8), with low heat transfer rates on the inlet and back side and higher rates on the outlet side, where the hydrogen flame reaches higher transfer rates across the entire crucible surface (cf. Figure 8, top and bottom). On the outlet side, the transfer rates can exceed those of the front side, leading to high standard deviations of 28 (hydrogen) and 22 kW/m^2 (methane), observed in the distribution function. Compared to the increase in the absolute amount of heat transferred by 19.0%, the standard deviation in the hydrogen case rises disproportionately by 27.3%. This describes a stronger scattering of the heat flux on the crucible surface around its mean value and thus a more uneven heat flux distribution, mainly due to the very high maximum transfer rates on the outlet side. Therefore, in the hydrogen case, more uneven melt bath temperatures and higher thermal stresses can be expected.

In summary, a significantly increased fuel utilization (19.0%) and thus higher energy efficiency can be observed during hydrogen operation, which could almost exclusively be attributed to an increased radiant heat share. The higher heat transfer rates could clearly be assigned to the outlet side, resulting in a significantly worse heat flux distribution. Furthermore, the net radiation power of the gases in both simulations is identified as the main influencing factor on the behavior of heat transfer to the crucible. In turn, this strongly depends on the temperature as well as the absorption and emission coefficients, which differ

significantly for both flames (radiation H_2O and CO_2). In Section 3 (cf. Figures 5 and 6), the increased net radiation of the hydrogen case was related to the higher temperatures compared to the methane flame, which is also identified as the main cause of the increased energy utilization rate and poorer heat distribution.

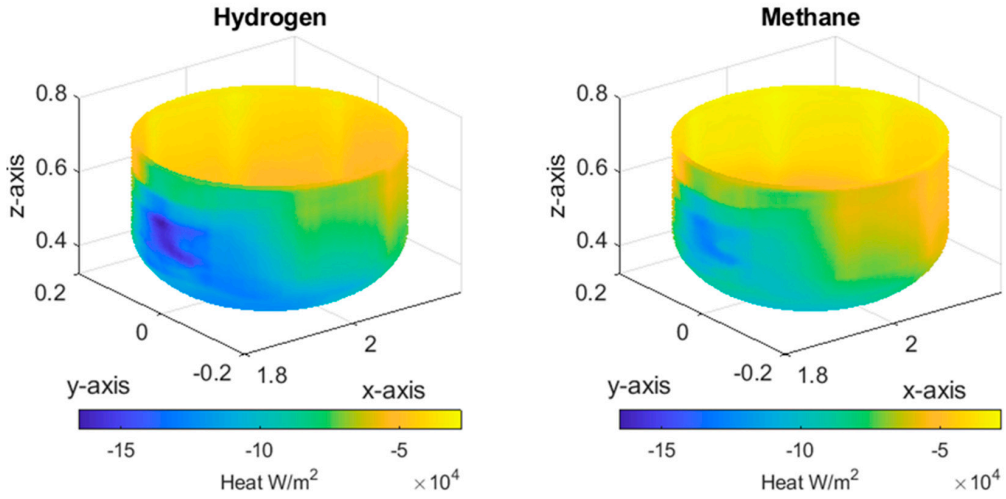

Figure 8. Absolute heat flux distribution into the crucible for the hydrogen (**left**) and methane flame (**right**).

With higher and more uneven heat transfer rates into the crucible, thermal stresses in the material increase, and more uneven melt bath temperatures are to be expected. Furthermore, higher temperatures can lead to an exponential increase in NOx emissions, which may exceed legal limits. For robust and compliant operation, measures such as increased air numbers or exhaust gas recirculation may be necessary to reduce combustion temperatures or further adjustments. How energy efficiency behaves with the implementation of measures aimed at reducing combustion temperatures remains to be evaluated. The results presented here suggest that radiation heat transfer rate into the crucible and thus energy efficiency should decrease with reduced temperatures.

4. Outlook

In this publication, a hydrogen and a methane flame with identical firing power were simulated in a crucible furnace at a steady-state operating point at 680 °C, describing the end of a melting run. Switching the fuel from methane to hydrogen significantly changes the temperature and flow fields as well as the heat transfer behavior into the crucible. Increased furnace chamber temperatures for the hydrogen case were determined, which could predominantly be attributed to the front and outlet sides. Furthermore, maximum temperatures and flame characteristics could be successfully corroborated with results from the literature.

An increased fuel utilization rate could be determined, which led to a 19.0% higher absolute heat flux into the crucible, which could allow for shorter heating times or a reduction in power. The higher heat flux could predominantly be attributed to the radiative heat part and the over-proportional increase in temperatures compared to methane starting at about 1550 K (cf. Figures 6 and 7). Simultaneously, a disproportional worsening of the spatially distributed heat transfer rate was determined (increase of the standard deviation by 27.3%).

Furthermore, the evaluation results indicate that measures to reduce combustion temperatures—such as exhaust gas recirculation, leaner operation to reduce NOx emissions, or compliance with temperature limits of materials—should result in a decreasing fuel utilization rate and more evenly distributed heat flux into the crucible. Additionally, constructive adjustments to the combustion chamber geometry, such as repositioning the

outlet or extending the burner introduction, could increase the residence time of the hot exhaust gases in the furnace and thereby increase fuel utilization.

To further examine the conclusions of this publication, future research could focus on a more extensive parameter study, systematically investigating the aforementioned influencing parameters (e.g., firing rate, air number, burner and furnace geometry) and comparing them to the original fossil-fuel-fired configuration. Additionally, the model could be developed to be fully transient to be able to describe the full transient heating up case, aiming to quantify the fuel utilization rate over the whole heating process.

Author Contributions: Investigation A.M.; project administration A.M.; conceptualization, A.M.; data curation, A.M.; methodology A.M.; writing—original draft preparation, A.M.; writing review and editing, A.M. supervision A.S. All authors have read and agreed to the published version of the manuscript.

Funding: This research was funded by the Ministry of Economic Affairs, Labour, and Tourism Bade-Württemberg, grant number [BW1_0176/02].

Data Availability Statement: All data and materials are available on request from the corresponding author. The data are not publicly available due to ongoing researches using a part of the data.

Acknowledgments: The authors would like to thank the Project Management Invest BW and the Ministry of Economic Affairs, Labour and Tourism Bade-Württemberg, who supported and supervised the research project. Furthermore: the authors acknowledge support by the state of Baden-Württemberg through bwHPC.

Conflicts of Interest: The authors declare that they have no conflicts of interest.

References

1. Qazi, U.Y. Future of Hydrogen as an Alternative Fuel for Next-Generation Industrial Applications; Challenges and Expected Opportunities. *Energies* **2022**, *15*, 4741. [CrossRef]
2. DECHEMA and acatech (Ed.) *A Comparison of International Hydrogen Strategies*; Country Analysis: Frankfurt, Germany, 2024. (In German)
3. Umann, U. Climate Targets: US Government Takes Environmental Protection Seriously. Available online: https://www.gtai.de/de/trade/usa/specials/klimaziele-us-regierung-nimmt-umweltschutz-ernst-808458 (accessed on 13 July 2024). (In German)
4. Frenz, W. EU Climate Law. In *Klimaschutzrecht: EU-Klimagesetz, KSG Bund und NRW, BEHG, Steuerrecht, Querschnittsthemen*; Frenz, W., Ed.; Erich Schmidt Verlag GmbH & Co. KG: Berlin, Germany, 2022; pp. 427–524. (In German)
5. Federal Republic of Germany. Federal Climate Protection Act (CPA). Available online: https://www.gesetze-im-internet.de/impressum.html (accessed on 23 May 2023). (In German)
6. Federal Ministry for the Environment, Nature Conservation and Nuclear Safety. The Climate Action Plan 2050—Germany's Long-Term Climate Protection Strategy. Available online: https://www.bmu.de/themen/klima-energie/klimaschutz/nationale-klimapolitik/klimaschutzplan-2050/ (accessed on 15 April 2021). (In German)
7. Federal Ministry for Economic Affairs and Climate Protection. What does "Efficiency First" Actually Mean? Available online: https://www.bmwi-energiewende.de/EWD/Redaktion/Newsletter/2016/23/Meldung/direkt-erklaert.html (accessed on 17 October 2022). (In German)
8. Hübner, T.; Guminski, A.; Rouyrre, E.; von Roon, S. *Energy Transition in Industry: Potential and Interactions with the Energy Sector*; FfE: München, Germany, 2019. (In German)
9. Schmidt, J.; Schlüter, W. *A Dynamic Process Simulation Model for the Energy Analysis of Aluminium Smelting Furnaces in a Comprehensive Material Flow Simulation*; GI Fachgruppen STS und GMMS: Lippstadt, Germany, 2016; pp. 29–37. (In German)
10. Hasankhani, M.; van Engelen, J.; Celik, S.; Diehl, J.C. Unveiling complexity of hydrogen integration: A multi-faceted exploration of challenges in the Dutch context. *J. Clean. Prod.* **2024**, *434*, 139927. [CrossRef]
11. Giacomazzi, E.; Troiani, G.; Di Nardo, A.; Calchetti, G.; Cecere, D.; Messina, G.; Carpenella, S. Hydrogen Combustion: Features and Barriers to Its Exploitation in the Energy Transition. *Energies* **2023**, *16*, 7174. [CrossRef]
12. Mayrhofer, M.; Koller, M.; Seemann, P.; Prieler, R.; Hochenauer, C. Assessment of natural gas/hydrogen blends as an alternative fuel for industrial heat treatment furnaces. *Int. J. Hydrogen Energy* **2021**, *46*, 21672–21686. [CrossRef]
13. Erler, F.; Röthig, P.; Werschy, M. Behaviour with Volatile Hydrogen Components: Investigation of the Behaviour of Existing Systems (Heating and CHP Appliances) under High, Volatile Hydrogen Quantities (0–40 vol.%) in Natural Gas. Available online: https://www.dbi-gruppe.de/files/PDFs/Dokumente/11_GWB/191220_Abschlussbericht_GWB_Wasserstoff.pdf (accessed on 10 June 2023). (In German)

14. Müller-Syring, G.; Henel, M. Hydrogen tolerance of the natural gas infrastructure including all associated systems. In *Abschlussbericht. Hg. v.*; DVGW Deutscher Verein des Gas-und Wasserfaches eV Technisch-wissenschaftlicher Verein: Bonn, Germany, 2014. (In German)
15. Foundry Technologies & Engineering GmbH (FT&E), Crucible Furnace. Available online: https://www.giessereilexikon.com/giesserei-lexikon/Encyclopedia/show/tiegelofen-866/?cHash=2f13bdf0587ee76b52dd2c3911010a34 (accessed on 7 February 2024). (In German)
16. Cherkaskyy, M.; Esche, A.; Fanghänel, C.; Schlegel, A. Energy Efficiency Potential in Planning Using the Foundry Industry as an Example: Study Commissioned by the Saxon State Ministry for the Environment and Agriculture. Chemnitz, Dresden, Augsburg und Zittau, 2015. Available online: https://tubaf.qucosa.de/api/qucosa:36055/attachment/ATT-0/ (accessed on 28 February 2023). (In German)
17. Herrmann, C.; Pries, H.; Hartmann, G. *Energy and Resource-Efficient Production of Aluminium Die Casting*; Springer: Berlin/Heidelberg, Germany, 2014. (In German)
18. Kuehn, T.H.; Goldstein, R.J. Numerical solution to the Navier-Stokes equations for laminar natural convection about a horizontal isothermal circular cylinder. *Int. J. Heat Mass Transf.* **1980**, *23*, 971–979. [CrossRef]
19. Mages, A.; Sauer, A. Comparison of numerical simulations of crucible furnaces for the description of energy-relevant operating conditions. *Z. Für Wirtsch. Fabr.* **2023**, *118*, 583–588. [CrossRef]
20. Wang, J.-M.; Yan, H.-J.; Zhou, J.-M.; Li, S.-X.; Gui, G.-C. Optimization of parameters for an aluminum melting furnace using the Taguchi approach. *Appl. Therm. Eng.* **2012**, *33*, 33–34. [CrossRef]
21. Ilbas, M.; Yılmaz, I.; Veziroglu, T.N.; Kaplan, Y. Hydrogen as burner fuel: Modelling of hydrogen–hydrocarbon composite fuel combustion and NOx formation in a small burner. *Int. J. Energy Res.* **2005**, *29*, 973–990. [CrossRef]
22. Ziani, L.; Chaker, A.; Chetehouna, K.; Malek, A.; Mahmah, B. Numerical simulations of non-premixed turbulent combustion of CH_4–H_2 mixtures using the PDF approach. *Int. J. Hydrogen Energy* **2013**, *38*, 8597–8603. [CrossRef]
23. Cellek, M.S.; Pınarbaşı, A. Investigations on performance and emission characteristics of an industrial low swirl burner while burning natural gas, methane, hydrogen-enriched natural gas and hydrogen as fuels. *Int. J. Hydrogen Energy* **2018**, *43*, 1194–1207. [CrossRef]
24. Bouziane, A.; Alami, A.; Zaitri, M.; Bouchame, B.; Bouchetara, M. Investigation of Swirl Stabilized CH_4 Air Flame with Varied Hydrogen Content by using Computational Fluid Dynamics (CFD) to Study the Temperature Field and Flame Shape. *Eng. Technol. Appl. Sci. Res.* **2021**, *11*, 6943–6948. [CrossRef]
25. Pashchenko, D. Hydrogen-rich fuel combustion in a swirling flame: CFD-modeling with experimental verification. *Int. J. Hydrogen Energy* **2020**, *45*, 19996–20003. [CrossRef]
26. Capurso, T.; Ceglie, V.; Fornarelli, F.; Torresi, M.; Camporeale, S.M. CFD analysis of the combustion in the BERL burner fueled with a hydrogen-natural gas mixture. *E3S Web Conf.* **2020**, *197*, 10002. [CrossRef]
27. Jenkins, B.; Mullinger, P. *Industrial and Process Furnaces: Principles, Design and Operation*; Butterworth-Heinemann: Oxford, UK, 2022.
28. Kroner, K.; Wicker, M. Air/gas Ratio Control on Industrial Heating Systems, Gaswärme International: Essen, Germany, 2006. Available online: https://docplayer.org/storage/66/55895674/1721465023/my0FbuJ5Ioqvxtvvlk JiYQ/55895674.pdf (accessed on 15 April 2024). (In German)
29. Zhou, B.; Yang, Y.; Reuter, M.A.; Boin, U.M.J. CFD-based process modelling of a rotary furnace for aluminium scrap melting. *Prog. Comput. Fluid Dyn.* **2007**, *7*, 195. [CrossRef]
30. Wittenschläger, T.; Degen, D.; Uhlig, V.; Trimis, D.; Reimann, T. *Optimisation of an Aluminium Melting Furnace Using Numerical Simulation*; Gaswärme International: Essen, Germany, 2013. (In German)
31. Wang, J.-M.; Xu, P.; Yan, H.-J.; Zhou, J.-M.; Li, S.-X.; Gui, G.-C.; Li, W.-K. Burner effects on melting process of regenerative aluminum melting furnace. *Trans. Nonferrous Met. Soc. China* **2013**, *23*, 3125–3136. [CrossRef]
32. Versteeg, H.K.; Malalasekera, W. *An Introduction to Computational Fluid Dynamics: The Finite Volume Method*; Pearson Education: Upper Saddle River, NJ, USA, 2007.
33. Panne, T. Characterisation of Numerical Methods for the Design of FLOX-Based Combustion Chamber Systems, University of Stuttgart, Stuttgart, Germany 2015. Available online: https://elib.dlr.de/102818/1/Druck_Version.pdf (accessed on 20 July 2024). (In German)
34. Yilmaz, D.; Onbasioglu, S.U.; Gökalp, I. Computational modeling of hydrogen enriched non premixed turbulent methane air flames. In Proceedings of the European Combustion Meeting (ECM), Louvain-la-Neuve, Belgium, 3–6 April 2005; pp. 3–6.
35. Minkowycz, W.J.; Sparrow, E.M.; Murthy, J. (Eds.) *Handbook of Numerical Heat Transfer*, 2nd ed.; Wiley: Hoboken, NJ, USA, 2008.
36. Fluent, A. *Ansys Fluent Theory Guide*; Ansys Inc.: Canonsburg, PA, USA, 2023.
37. *Heat Transport Phenomena and Heat and Mass Transfer*; Working documents for the lectures; Technical University of Munich: München, Germany, 2017. (In German)